AGU PUBLICATIONS

JGR

Journal of Geophysical Research: Oceans

RESEARCH ARTICLE

10.1002/2016JC012406

Key Points:
- Our data assimilation system provided a time-varying estimate of physical fields, colored dissolved organic matter, and SF_6 tracers
- Mixing and photodegradation were the predominant factor controlling the distribution of colored dissolved organic matter over the period of the field experiment
- Regional data assimilation systems can be used in the planning and execution of process studies

Correspondence to:
C. E. Del Castillo,
carlos.e.delcastillo@nasa.gov

Citation:
Del Castillo, C. E., S. Dwivedi, T. W. N. Haine, and D. T. Ho (2017), Estimating the distribution of colored dissolved organic matter during the Southern Ocean Gas Exchange Experiment using four-dimensional variational data assimilation, *J. Geophys. Res. Oceans*, *122*, 2029–2049, doi:10.1002/2016JC012406.

Received 30 SEP 2016
Accepted 6 FEB 2017
Accepted article online 11 FEB 2017
Corrected 16 MAR 2017

This article was corrected on 31 MAR 2017. See the end of the full text for details.

Estimating the distribution of colored dissolved organic matter during the Southern Ocean Gas Exchange Experiment using four-dimensional variational data assimilation

C. E. Del Castillo[1,2], S. Dwivedi[3], T. W. N. Haine[2], and D. T. Ho[4]

[1]Ocean Ecology Laboratory, National Aeronautics and Space Administration, Goddard Space Flight Center, Greenbelt, Maryland, USA, [2]Department of Earth and Planetary Sciences, Johns Hopkins University, Baltimore, Maryland, USA, [3]Department of Atmospheric and Ocean Sciences, University of Allahabad, Allahabad, India, [4]Department of Oceanography, University of Hawaii, Honolulu, Hawaii, USA

Abstract We diagnosed the effect of various physical processes on the distribution of mixed-layer colored dissolved organic matter (CDOM) and a sulfur hexafluoride (SF_6) tracer during the Southern Ocean Gas Exchange Experiment (SO GasEx). The biochemical upper ocean state estimate uses in situ and satellite biochemical and physical data in the study region, including CDOM (absorption coefficient and spectral slope), SF_6, hydrography, and sea level anomaly. Modules for photobleaching of CDOM and surface transport of SF_6 were coupled with an ocean circulation model for this purpose. The observed spatial and temporal variations in CDOM were captured by the state estimate without including any new biological source term for CDOM, assuming it to be negligible over the 26 days of the state estimate. Thermocline entrainment and photobleaching acted to diminish the mixed-layer CDOM with time scales of 18 and 16 days, respectively. Lateral advection of CDOM played a dominant role and increased the mixed-layer CDOM with a time scale of 12 days, whereas lateral diffusion of CDOM was negligible. A Lagrangian view on the CDOM variability was demonstrated by using the SF_6 as a weighting function to integrate the CDOM fields. This and similar data assimilation methods can be used to provide reasonable estimates of optical properties, and other physical parameters over the short-term duration of a research cruise, and help in the tracking of tracer releases in large-scale oceanographic experiments, and in oceanographic process studies.

1. Introduction

This study was motivated by the limitations of remote sensing coverage due to cloud interference during the Southern Ocean Gas Exchange experiment (SO GasEx), and our need to understand biophysical processes controlling the distribution of inherent optical properties (IOPs) in the ocean. It was also motivated by difficulties in predicting the trajectory of tracers released during SO GasEx. Therefore, our goals were to estimate the three-dimensional time evolving distribution of colored dissolved organic matter (CDOM) during SO GasEx, diagnose the physical processes controlling CDOM distribution, and to determine the skill of our model in predicting the trajectory of a tracer patch.

This study takes advantage of previous efforts by *Del Castillo and Miller* [2011], *Dwivedi et al*. [2011], and *Ho et al*. [2011]. They, respectively, documented CDOM distribution, sources, and sinks during SO_GasEx, presented a state estimate of the physical (circulation, hydrographic, and mixed-layer) fields during SO GasEx, and presented results of sulfur hexafluoride (SF_6) and helium-3 (^{3}He) tracer releases to better parameterize air-sea gas exchange in the Southern Ocean.

Here we hypothesized that thermocline entrainment, photodegradation, and advection controlled the mixed-layer CDOM at the study site. Entrainment decreases mixed-layer CDOM because thermocline CDOM values are lower than those in the mixed-layer. Photodegradation is a sink, whereas advection can act as either a source or a sink of CDOM. Biological sources and sinks of CDOM are important in the SO and elsewhere [e.g., *Nelson et al*., 1998; *Del Castillo and Miller*, 2011]. However, they are uncertain in magnitude and we hypothesize that are negligible in comparison to physical processes over periods of weeks (recall that our ultimate goal is to use models to fill gaps in satellite imagery, which are typically in the order of days).

To test our hypothesis, we performed several numerical experiments designed to constrain the effects of photobleaching, entrainment, and advection on CDOM as quantified in a state estimate. A successful fit of the modeled CDOM fields to the data means that biological processes are negligible over the course of the experiment. Furthermore, we hypothesized that our data assimilation model will show skill in describing the dispersal of SF_6 tracer.

The SO GasEx took place in the South Atlantic Ocean near South Georgia Island during the austral fall of 2008 (29 February to 12 April 2008) [*Ho et al*., 2011]. The main objectives of SO GasEx were to measure and quantify air-sea gas transfer velocities at high wind speeds, and to understand the influence of chemical and biological processes on gas exchange. As part of this task, SF_6 and ^3He were released in the mixed-layer and their dispersal was mapped.

In general, CDOM abundances in the Southern Ocean are low. Expressed as the absorption coefficient (a_g) at 440 nm, values in the literature are typically 0.02 m^{-1}, but generally higher in our study site (average 0.046 m^{-1}; $\sigma = 0.01$) [see *Del Castillo and Miller*, 2011, and references therein]. Higher absorption coefficients are found in coastal waters, and in particular, the region around South Georgia Island, near the SO GasEx study site, had high CDOM (a_g (440) $\sim$ 0.05 m^{-1}) and chlorophyll [*Del Castillo and Miller*, 2011]. High values of chlorophyll are attributed to the island mass effect [*Atkinson et al*., 2001; *Korb and Whitehouse*, 2004; *Meskhidze et al*., 2007]. *Del Castillo and Miller* [2011] describe vertical and horizontal variability of CDOM during SO GasEx and conclude that high values of CDOM in the study region could be caused by either in situ production or by runoff from South Georgia Island. The typical values of a_{CDOM} (440) in the region ranged from $\sim$0.02 to $\sim$0.06 m^{-1} [*Del Castillo and Miller*, 2011].

The processes controlling the spatial and temporal distribution of upper ocean CDOM in the study region are largely unknown and the cruise track sparsely sampled the region (Figure 1). For this reason, synthesizing data with a regional model using data assimilation is an attractive way to study the CDOM dynamics. In a previous contribution [*Dwivedi et al*., 2011], we described and presented a state estimate of the physical (circulation, hydrographic, mixed-layer) fields during SO GasEx. Here we extend that study by including CDOM data from both in situ samples and satellite observations. The SF_6 data were also included.

2. State Estimation

The state estimation requires a limited area eddy-resolving numerical ocean circulation model, an assimilation procedure, observations, and their associated uncertainties. The ocean circulation model used was the MITgcm, and the method of Lagrange multipliers produced a least square fit of the model to the data [*Dwivedi et al*., 2011]. The discrepancy between the model trajectory and the observations was minimized using an iterative algorithm.

Below we describe in brief the ocean circulation model setup. Further details of the forward and adjoint models are given in *Dwivedi et al*. [2011]. We customized the MITgcm to run at high-resolution in the area (35.09°W–40.41°W, 49.65°S–52.85°S) around the SO GasEx cruise region (36.88°W–38.58°W, 50.71°S–51.79°S), and used the zonally periodic boundary condition (Figure 1). We used spherical polar coordinates with approximately 4 km ($\sim$0.065°) horizontal resolution in the SO GasEx domain. The model has 36 vertical (depth) levels (Table 1). We used higher vertical resolution for the upper ocean (5 m for the top 50 m) slowly telescoping out at depth. The bathymetry data were extracted from the high-resolution topography data of *Smith and Sandwell* [1997]. The 6 hourly air temperature, humidity, precipitation, evaporation, and downwelling longwave radiation data from the NCEP/NCAR reanalysis [*Kalnay et al*., 1996] were used to force the model. The wind speeds 10 m above sea level were taken from the blended sea winds data [*Zhang et al*., 2006]. For downward shortwave radiation forcing, we used hourly surface solar irradiance obtained from the OASIM model [*Gregg and Casey*, 2009]. We developed packages to simulate the advection and diffusion of CDOM and SF_6 tracers [sections 2.1 and 2.2] and couple them to the MITgcm passive tracer package [*Adcroft et al*., 2009]. The circulation model was started with an initial hydrography (temperature and salinity), initial horizontal velocity, and initial sea level elevation field. These initial fields were obtained from the SO GasEx state estimate (GESE) of *Dwivedi et al*. [2011].

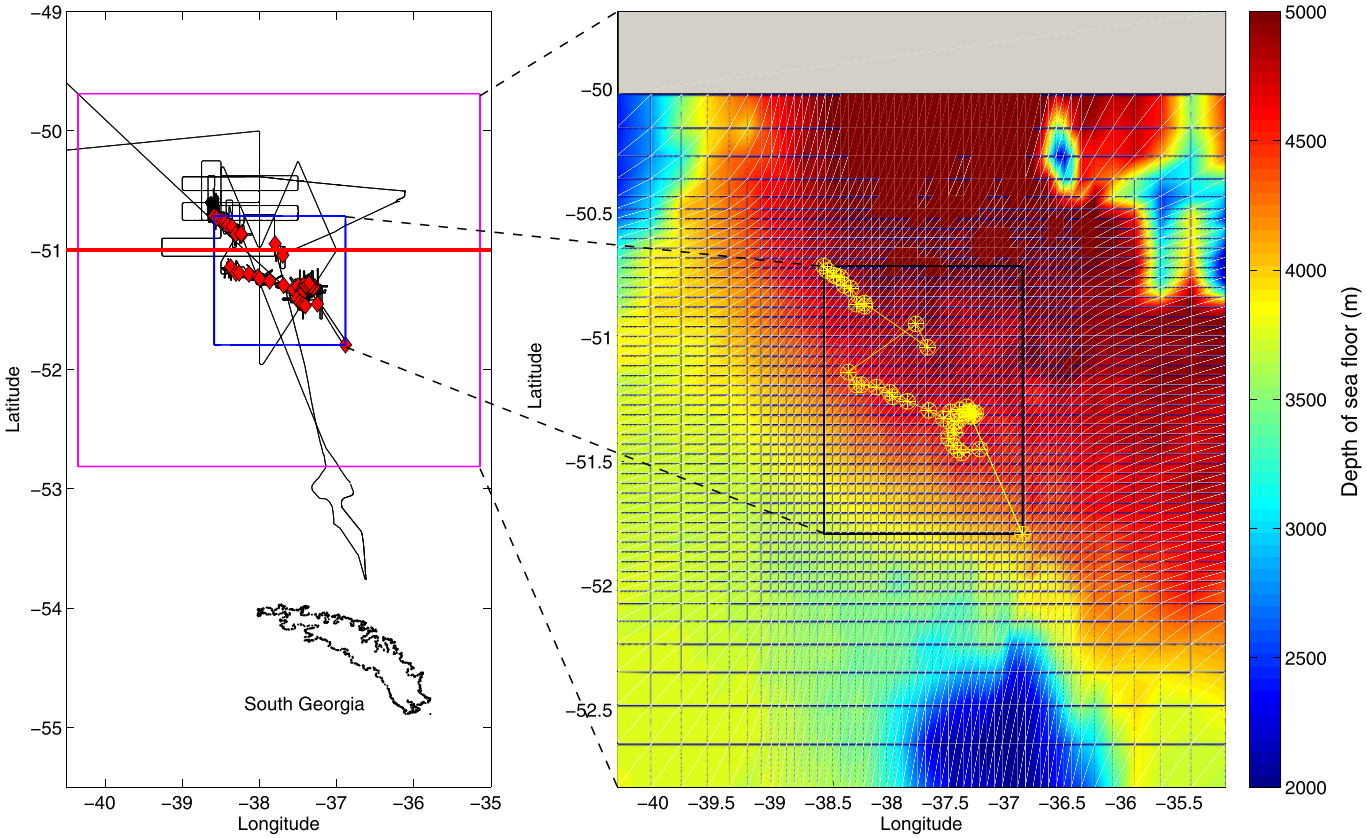

Figure 1. Cruise track and location of CTD stations that included CDOM samples (shaded diamonds). Mixed-layer CDOM values doubled south of 51°S for stations sampled after 20 March 2008 (thick latitude line). The regional model domain is shown on the right and is periodic in the zonal direction (the gray bar shows the northern wall). The region of interest for SO GasEx is the central rectangle surrounding the CTD stations.

In the 4-D Var assimilation technique, we minimized a scalar cost function (J), which is the sum of squared model-data misfit terms, and squared control-vector correction terms, with every term appropriately weighted:

$$J=\left\{\sum_{t=1}^{t_f}\left[\boldsymbol{y}(t)-\boldsymbol{E}(t)\boldsymbol{x}(t)\right]^T\boldsymbol{R}^{-1}\left[\boldsymbol{y}(t)-\boldsymbol{E}(t)\boldsymbol{x}(t)\right]\right\}+\left[\boldsymbol{x}(0)-\boldsymbol{x}_0^b\right]\boldsymbol{P}_0^{-1}\left[\boldsymbol{x}(0)-\boldsymbol{x}_0^b\right], \quad (1)$$

where the first sum represents the model-data misfit terms, and the second term represents initial-condition uncertainty. In (1), $\boldsymbol{x}(t)$ is the model state vector at time step t; $\boldsymbol{y}(t)$ is the vector of observations; $\boldsymbol{E}(t)\boldsymbol{x}(t)$ is the corresponding model counterpart; and $\boldsymbol{x}_0^b$ is the background estimate of the model state at the initial time. $\boldsymbol{R}$ here is the error covariance matrix for the data-model misfit terms, and $\mathbf{P}_0$ is the background error covariance matrix for initial state $\boldsymbol{x}_0^b$ [*Dwivedi et al.*, 2011]. The assimilation process controls the initial temperature and salinity, initial horizontal velocity, initial SF_6 concentration, and initial CDOM absorption coefficients at 350, 380, and 400 nm. The length of the control vector is 790,328 for these eight variables. The cost function that is minimized included contributions from the in situ data, remotely sensed data, and initial fields. The in situ data terms in the cost function were due to CTD temperature and salinity (CTDT and CTDS), CDOM at 350 nm (CDOM350), CDOM380, CDOM400, and deliberately released and background SF_6. The remotely sensed satellite data terms in the cost function were due to the sea surface temperature (SST), normalized absolute dynamic topography (NADT), surface CDOM at 350 nm (SCDOM350), SCDOM380, and SCDOM400 fields. The initial temperature, salinity, CDOM (at each wavelength), and SF_6 fields also contributed to the cost function. These observations are described in detail in section 3. Adjusting the surface forcing was not needed to achieve a close fit to the data over a period of 26 days.

Table 1. Model Vertical Levels, Thicknesses, and Depths

Vertical (z) Level	Thickness (m)	Depth (Middle of the Cell) (m)
1	5	2.5
2	5	7.5
3	5	12.5
4	5	17.5
5	5	22.5
6	5	27.5
7	5	32.5
8	5	37.5
9	5	42.5
10	5	47.5
11	6	53.0
12	6	59.0
13	6	65.0
14	6	71.0
15	7	77.5
16	9	85.5
17	11	95.5
18	14	108.0
19	18	124.0
20	22	144.0
21	28	169.0
22	35	200.5
23	45	240.5
24	55	290.5
25	70	353.0
26	90	433.0
27	120	538.0
28	150	673.0
29	200	848.0
30	250	1073.0
31	350	1373.0
32	500	1798.0
33	650	2373.0
34	800	3098.0
35	1000	3998.0
36	1000	4998.0

2.1. CDOM Modeling

We developed a package for MITgcm to simulate advection and diffusion of CDOM at multiple wavelengths. We treated the CDOM absorption coefficients as passive tracers with time and space-varying sources and sinks. The absorption of light by CDOM and the associated photobleaching (photolysis) acted as the main sink. Following *Del Vecchio and Blough* [2002], the CDOM absorption coefficient a_{CDOM} after illumination for a short time Δt is

$$a_{CDOM}(\lambda, z) = a_{CDOM}(\lambda) \exp[-f(I, z)Dt], \quad (2)$$

where $f(\lambda, z)$ is the photobleaching rate at wavelength λ and depth z. It is given by

$$f(\lambda, z) = \sigma_P(\lambda)E(\lambda)\exp[-k(\lambda, z)z], \quad (3)$$

where $\sigma_P(\lambda)$ is the photobleaching cross-section (from *Del Vecchio and Blough* [2002], which takes into account indirect photobleaching), $E(\lambda)$ is the solar irradiance at wavelength λ transmitted through the sea surface, and $k(\lambda, z)$ is the vertical attenuation coefficient, which for computational simplicity was approximated as 1.3 $a_{g,w}(\lambda, z)$ [*Preisendorfer*, 1976], $a_{g,w} = a_g(\lambda) + a_w(\lambda)$, and $a_w(\lambda)$ is the absorption by pure water [*Smith and Baker*, 1981]. In previous work, we have found this to be a reasonable approximation for k, particularly in water with optical properties dominated by CDOM absorbance [*Del Castillo et al.*, 1999].

The CDOM model was run for three different wavelengths 350, 380, and 400 nm using the hourly surface solar irradiance obtained from the OASIM radiative transfer model. The OASIM model provides realistic solar irradiance values. See *Gregg and Casey* [2009] for a detailed discussion.

The CDOM background initial conditions were made by combining satellite and in situ CDOM data for each wavelength. The average vertical profile of in situ CDOM observations was scaled at each horizontal point to match the average surface SCDOM observations from the satellite. For each wavelength modeled, we took the average vertical profile of CDOM data from the in situ water samples (section 3.2). Then we took the time average surface SCDOM observations from satellite data (section 3.3). The CDOM background initial-condition field was then computed by projecting the average surface values into the water column using the average vertical profile adjusted so that it matches the surface values at every place.

2.2. SF_6 Modeling

The SF_6 concentration field was treated as a passive tracer with air-sea gas exchange. The air-sea SF_6 flux was calculated as

$$F_{exch} = k_p(FX_{atm} - X_{surf}), \quad (4)$$

where k_p is the gas transfer velocity, F is the SF_6 solubility, and X_{atm} and X_{surf} are the SF_6 concentrations in the atmospheric boundary layer and at the ocean surface, respectively. The k_p and F parameters were obtained following the procedure of *Ho et al.* [2006] and X_{atm} is chosen as 6.2 pptv (http://www.esrl.noaa.gov/gmd/hats/combined/SF6.html).

Two SF_6 releases were made during the SO GasEx. The nominal injection depth for both releases was 5–6 m. The first injection took place on 8 March 2008 centered at 38.63°W, 50.60°S. The second injection

took place on 21 March 2008 and was centered at 38.40°W, 51.14°S. To simulate these events, we used two SF_6 tracer fields in the model. The first field was initialized with a small concentration of 5 fmol L^{-1} on 10 March 2008 (the start date of the state estimate). We then relaxed the tracer concentration in the mixed-layer to 2000 fmol L^{-1} at 38.40°W, 51.14°S on 21 March 2008. We denoted this tracer as SF_6_1: it represents the released SF_6. The second (referred to as SF_6_2) represents the prerelease SF_6 field and the weak SF_6 field from the 8 March 2008 test release. The SF_6_2 tracer starts on 10 March 2008 with an initial concentration obtained by averaging the observed SF_6 profiles between 10 and 21 March 2008. Both of the fields advected, diffused, and exchanged with the atmosphere during the simulation and the initial concentration of SF_6_2 was controlled by the optimization procedure. We computed the misfit between SF_6 observations and the sum of SF_6_1 and SF_6_2 to estimate the SF_6 cost.

3. Observations and Associated Uncertainties

Physical and biochemical measurements were used in the state estimate. The physical measurements included sea surface height and temperature from satellites and in situ hydrographic data. *Dwivedi et al.* [2011] also use these data and only a brief description is given here. The biochemical measurements (in situ and satellite CDOM and in situ SF_6) were new to this state estimate.

3.1. Sea Surface Height, Sea Surface Temperature, and In Situ Hydrography Observations

Remote-sensed sea surface height data were derived from Normalized Absolute Dynamic Topography (NADT) measurements. The NADT data were obtained by subtracting the space-time-mean dynamic topography—a single number—from the AVISO multimission gridded absolute dynamic topography data. This process ensured that the mean of NADT was zero. The AVISO formal mapping error field corresponding to the gridded data was used as the NADT uncertainty in the state estimate. There were 18,928 NADT observational data in the state estimate.

Remote-sensed sea surface temperature (SST) data were taken from the Advanced Very High Resolution Radiometer, Advanced Microwave Scanning Radiometer, Optimal Interpolation, L4, gridded data set from the Global Ocean Data Assimilation Experiment High Resolution Sea Surface Temperature Pilot Project (GHRSST-PP) [*Reynolds et al.*, 2007]. We chose a constant value of 1°C for SST uncertainty as in *Dwivedi et al.* [2011]. There were 18,928 SST observational data in the state estimate.

The in situ temperature and salinity (CTDT and CTDS) observations were obtained from the 41 CTD stations along the SO GasEx cruise track between 6 March and 4 April 2008. The uncertainty values of 0.4°C and 0.05 for CTDT and CTDS were used in the state estimate (as in *Dwivedi et al.* [2011]). There were 845 CTDT and CTDS observational data (each) in the state estimate.

3.2. In Situ CDOM Observations

In situ SO GasEx CDOM observations are discussed in detail by *Del Castillo and Miller* [2011]. Briefly, water samples for CDOM analysis were collected at 51 locations (Figure 1). Samples were drawn from the water bottles to cover the mixed-layer, thermocline, and several depths below the thermocline. Water was collected in clean amber-colored glass bottles and filtered through prerinsed 0.22 μm membrane filters under light vacuum. All samples were analyzed on board using an Ultrapath wave-guide spectrophotometer [*Miller et al.*, 2002]. Absorption scans were collected between 300 and 750 nm. The absorption coefficient, $a_{CDOM}(\lambda)$, was calculated using $a_{CDOM}(\lambda)=2.303A(\lambda)/l$, where A is the absorbance, and l is the path length in meters which was 2 m in this case. Corrections for the difference in refractive index between seawater and the blank were made according to *Nelson et al.* [2007]. The spectral slope parameter S was calculated between 350 and 500 nm using spectral observations and a least square regression [e.g., *Blough and Del Vecchio*, 2002]. Abundance of CDOM was reported using the absorption coefficient of CDOM at 440 nm (CDOM440) to ease comparison with remote sensing estimates of CDOM [*Zhu et al.*, 2011]. However, in the model described below we used $a_{CDOM}(\lambda)$ at 350, 380, and 400 nm because these wavelengths are more relevant to CDOM photochemistry [*Coble*, 2007; *Zhu et al.*, 2011]. A total of 504 in situ CDOM observations were used in the state estimate for each wavelength. The standard deviation of the difference between the raw CDOM and the gridded (bin-averaged) interpolated CDOM abundances was 0.01 m^{-1}. This value was used as the CDOM uncertainty for each wavelength. The space-time standard deviation of in situ CDOM

data was 0.05 m^{-1} for each wavelength. This value was used as the uncertainty of the initial (background) CDOM field at all grid points.

3.3. Satellite Surface CDOM Observations

Remote sensing imagery from the Moderate Resolution Imaging Spectrometer (MODIS-AQUA) was downloaded from NASA's Ocean Color web-site (http://oceancolor.gsfc.nasa.gov). Imagery from the Sea-viewing Wide Field of View Sensor (SeaWiFS) was not available for the cruise period. Remote sensing reflectance values was extracted from the imagery and we used the quasi-analytical algorithm of *Lee et al*. [2002] to calculate surface CDOM absorption coefficients at 448 nm (SCDOM448). The satellite retrievals at 412 nm were not used due to uncertainties with the atmospheric corrections at this wavelength. Owing to cloud cover, SCDOM448 observations were available for only 4 days (on 21, 22, 24, and 27 March 2008) within our simulation period. Moreover, none of these observations have complete coverage over the SO GasEx domain. For this reason, we were not able to perform a validation of the SCDOM448 retrieval using matchups with in situ data. However, the satellite retrievals were within the range of values obtained with in situ samples [see *Del Castillo and Miller*, 2011, for further discussion]. There were 1877 observations of SCDOM in the SO GasEx domain during the assimilation period.

The CDOM spectral slope $\overline{S}$ was used to calculate SCDOM350, SCDOM380, and SCDOM400 based on these remote sensing retrievals at 448 nm according to

$$SCDOM(\lambda) = SCDOM(\lambda_{ref})\ \exp[(\lambda_{ref}-\lambda)] \tag{5}$$

with $\lambda_{ref} = 488$ nm and $\overline{S} = 0.0145$ nm^{-1} ($\sigma = 0.0009$; ranged from 0.0138 to 0.0167 nm^{-1}). Here $\overline{S}$ is the average value of spectral slope from the entire in situ data, not just the surface samples. The SCDOM in the SO GasEx region varies between 0.03 and 0.003 m^{-1} for 448 nm, whereas it varies between 0.248 and 0.015 m^{-1} for 350 nm, between 0.156 and 0.009 m^{-1} for 380 nm, and between 0.114 and 0.007 m^{-1} for 400 nm, over the period of interest. The standard deviation of SCDOM is 0.04 m^{-1}, and this value was used as the SCDOM uncertainty for each wavelength in the state estimate.

3.4. In Situ SF_6 Observations

A total of 41 profiles of SF_6 were obtained from CTD stations between 10 March and 4 April 2008. During this period of 26 days, deliberately released SF_6 observations are available on 21 individual days (15–17, 19, and 21 March 2008 are missing). The in situ SF_6 data were bin-averaged and interpolated to the model grid, giving 697 observations in the state estimate. The SF_6 concentration in the SO GasEx region during the cruise period varied between 5 and 1200 fmol L^{-1}.

The space-time-varying uncertainty of the SF_6 data (σ) in the state estimate was obtained by taking into account both instrumental error as well as the least count error in observing the SF_6 concentration. We use

$$\sigma = \sqrt{(C\varepsilon)^2 + {\sigma_{th}}^2}, \tag{6}$$

where C is the SF_6 concentration, ε is the random instrumental error, chosen as 5%, and the instrumental threshold σ_{th} is 5 fmol L^{-1}. The standard deviation of all the in situ SF_6 data is 80 fmol L^{-1}. This value is used as the background uncertainty for the initial SF_6 field at all grid points in the state estimate.

4. Results and Discussion

We present the results in two stages: first, we compare the state estimate with the SO GasEx observations to gauge the quality of the model-data fit. Second, we quantify the mixed-layer entrainment and the effects of photobleaching, lateral advection, and diffusion to diagnose processes controlling mixed-layer CDOM. The detailed physical data assimilation in the SO GasEx region has been described in *Dwivedi et al*. [2011], so here we emphasize the results of CDOM and SF_6 tracers.

4.1. Quality of the State Estimate

We performed biochemical ocean state estimation for 26 days (10 March to 4 April 2008) in the SO GasEx cruise region using the method of Lagrange multipliers. 125 optimization iterations were performed to obtain a model trajectory that fits the observations and initial state guesses within their uncertainties

Table 2. Normalized Cost Function Contributions for Various Iterations in the GESE-CDOM Optimization

	Normalized Cost Function											
Iteration Number	Total	NADT	SST	CTDT	CTDS	SF_6	CDOM 350	CDOM 380	CDOM 400	SCDOM 350	SCDOM 380	SCDOM 400
0	1.00	1.00	1.00	1.00	1.00	1.00	1.00	1.00	1.00	1.00	1.00	1.00
25	0.33	0.81	0.75	0.27	0.35	0.24	0.09	0.09	0.09	0.55	0.63	0.52
50	0.28	0.81	0.73	0.18	0.29	0.19	0.07	0.06	0.06	0.52	0.60	0.49
75	0.25	0.70	0.72	0.15	0.24	0.16	0.07	0.06	0.06	0.49	0.57	0.47
100	0.24	0.68	0.70	0.14	0.22	0.15	0.06	0.06	0.06	0.48	0.55	0.45
125	0.23	0.67	0.69	0.13	0.20	0.15	0.06	0.06	0.06	0.48	0.54	0.45

(hereinafter called the SO GasEx state estimate with CDOM, GESE-CDOM). Table 2 summarizes various normalized cost function contributions against optimization iteration number. It is clear from the table that good convergence is obtained, and the total cost function, as well as the individual costs associated with each observation, reduces substantially in 125 iterations.

In Figure 2, we compare the time-mean GESE-CDOM sea level anomaly field with AVISO NADT observations (top plot) and the time-mean GESE-CDOM SST field with GHRSST-PP SST data (bottom plot) for the SO GasEx domain. Clearly, the GESE-CDOM solution matches with the overall observed sea level variations and

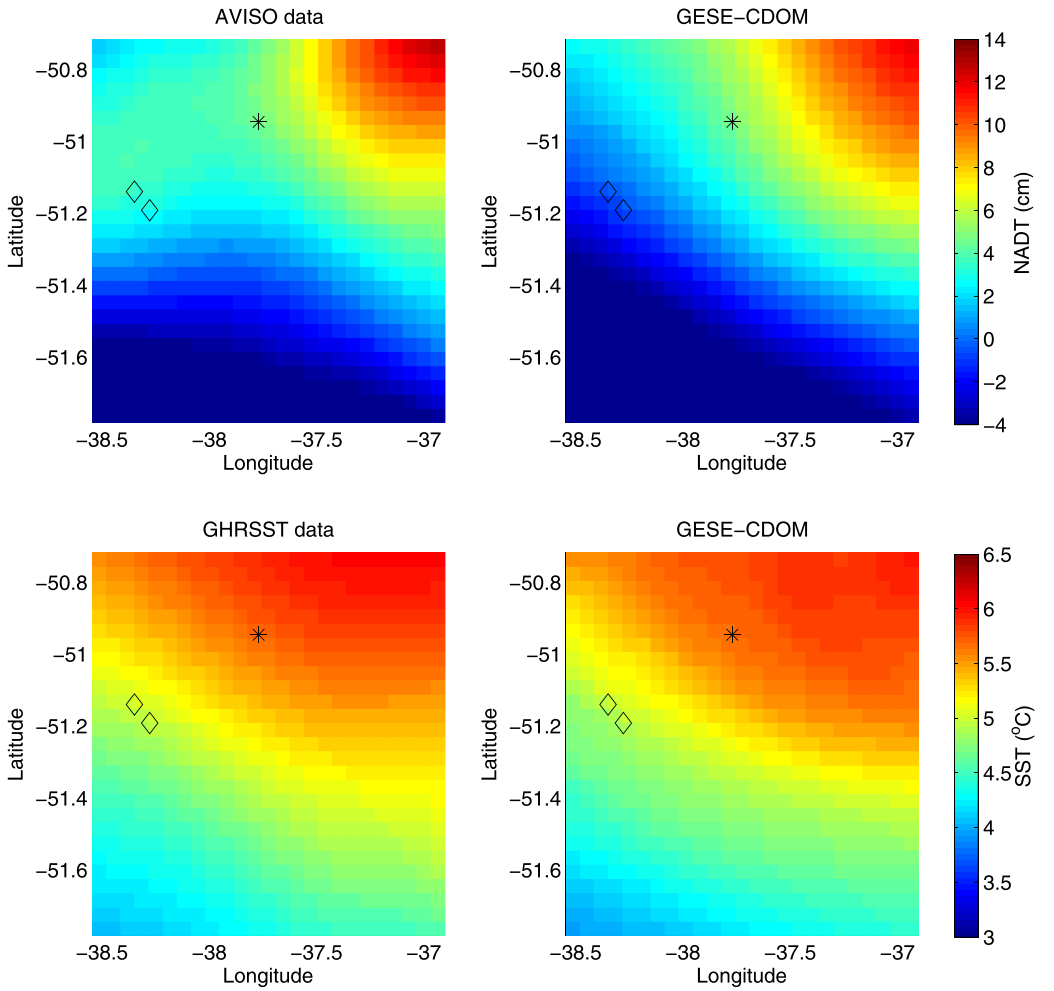

Figure 2. Comparison of the (top plot) time averaged normalized absolute dynamic topography (cm) from AVISO with the GESE-CDOM solution and, (bottom plot) time averaged SST (°C) from GHRSST with the GESE-CDOM solution. The time average is over the period 10 March to 4 April 2008 in the SO GasEx domain. The star and diamonds show the SO GasEx cruise station on 20 March and 22 March 2008, respectively. The cross marks the SF_6 injection site on 21 March 2008.

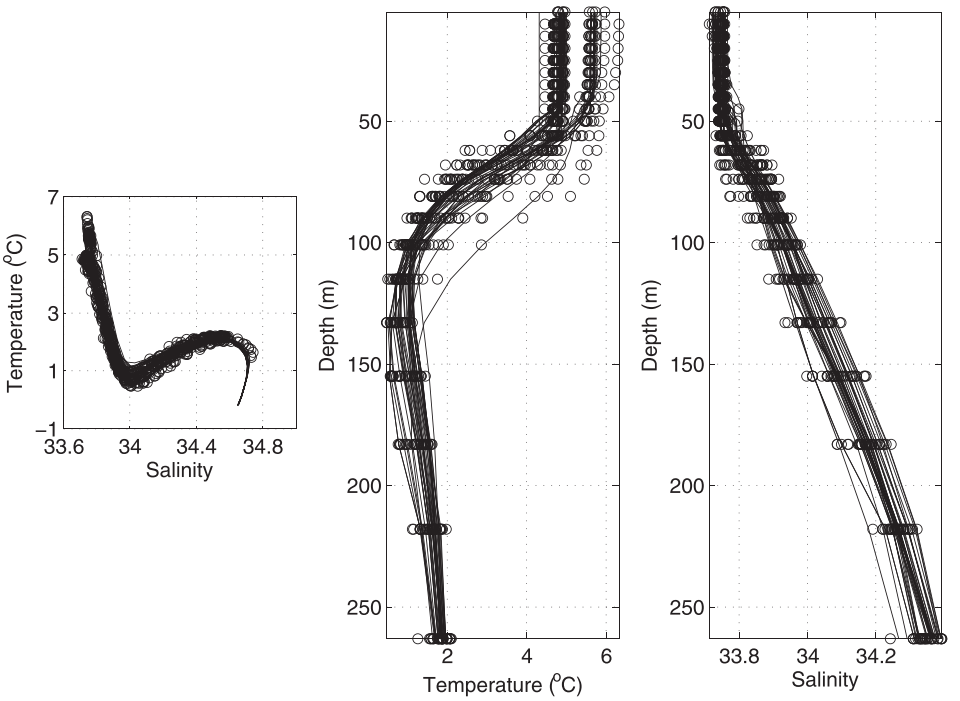

Figure 3. Comparison of the temperature and salinity values obtained from the GESE-CDOM solution (solid line) with the gridded in situ CTD data (circles) during SO GasEx (10 March to 4 April 2008). (left plot) temperature (°C) as a function of salinity. (middle plot) Temperature (°C) as a function of depth (m). (right plot) Salinity as a function of depth (m). Only the upper ocean (to 260 m) is shown in the middle and right plots.

SST of the SO GasEx region. The correlation and root mean square error (RMSE) between the AVISO NADT and the GESE-CDOM solution is 0.97 and 1.6 cm, respectively, whereas the correlation and RMSE between the GHRSST-PP SST and the corresponding GESE-CDOM SST field is 1.0 and 0.08°C, respectively. The RMSE in model-data fit of NADT and SST are small compared to the NADT error (15 cm) and SST error (1°C), respectively. We also measured daily variations in the NADT and SST estimates with respect to their corresponding observations. The space-time correlation between daily AVISO NADT data and daily GESE-CDOM NADT estimate was computed after removing the appropriate time-mean NADT from the fields. Similar analysis was also performed for the SST fields. We found that the space-time correlations for NADT and SST daily anomaly fields were 0.65 and 0.50, respectively. These correlations were significant at 99.9% level. Further details on the quality of GESE-CDOM NADT and SST fields are given in *Dwivedi et al*. [2011].

In Figure 3, we compare the in situ CTD temperature and salinity measurements with the corresponding GESE-CDOM profiles. The assimilated model solution reproduced the overall hydrographic structure of the SO GasEx region. Two clearly distinct temperature ranges were seen in the upper 50 m of the ocean, with very little fluid between 5 and 5.5°C (consistent with the SST front in Figure 2). The solution slightly underestimates the high temperatures in the mixed-layer (thermocline) region. On the other hand, it slightly overestimates the low temperatures in the thermocline region. Similarly, salinity values are also slightly overestimated in the thermocline region. The correlation (R value) and RMSE between the in situ and GESE-CDOM CTDT is 0.98 and 0.1°C, respectively. Similarly, the correlation and RMSE between the in situ and GESE-CDOM CTDS were 1.0 and 0.01, respectively. The RMSE in model-data fit of CTDT and CTDS was small compared to their uncertainty values of 0.2°C and 0.02, respectively.

In Figure 4, we compared the time-mean MODIS-AQUA derived SCDOM fields at 350, 380, and 400 nm with the corresponding GESE-CDOM SCDOM fields for the SO GasEx domain. The SCDOM values are lowest to the southwest with an abrupt transition to higher values in the central part of the domain. This transition also appears in NADT and SST (Figure 2) although it is less abrupt. The SCDOM is significantly correlated with NADT and SST. The correlation of SCDOM with NADT and SST is 0.5 and 0.6, respectively, whereas the

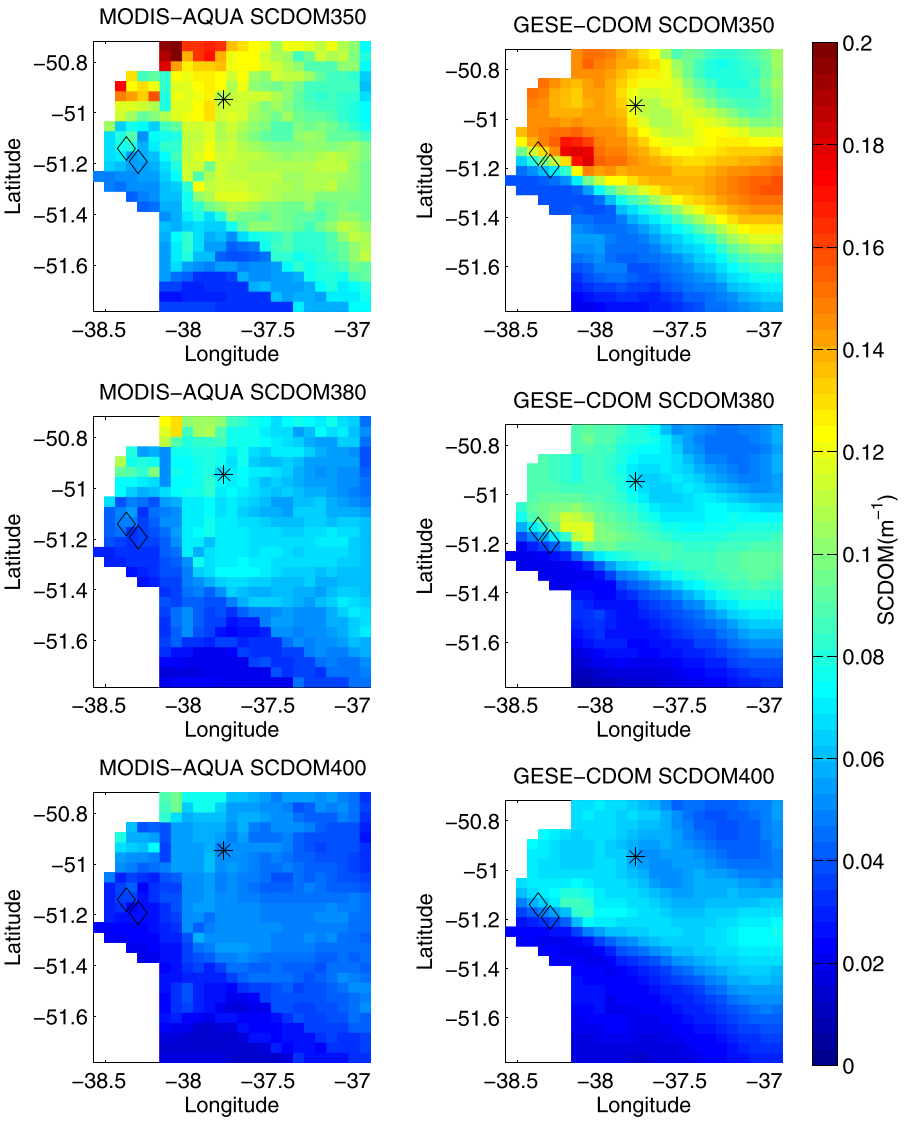

Figure 4. Comparison of the time averaged MODIS-AQUA derived SCDOM field at (top plot) 350 nm, (middle plot) 380 nm, and (bottom plot) 400 nm with the corresponding GESE-CDOM SCDOM fields for the SO GasEx domain. The time average is over 21, 22, 24, and 27 March 2008 (the dates of the satellite data). The star and diamonds show the SO GasEx cruise station on 20 March and 22 March 2008, respectively. The cross marks the SF_6 injection site on 21 March 2008.

correlation between SST and NADT is 0.9. High CDOM values associate with high sea level and a warm sea surface.

The GESE-CDOM matched the satellite CDOM surface fields (time averages over the dates with satellite cover) with a correlation of 0.7 and an RMSE of 0.01 m^{-1}. The model-data RMSE is small compared to the data uncertainty (0.04 m^{-1}). The GESE-CDOM, however, had a systematic high bias in the central part of the domain, and the frontal region is displaced toward the northeast (Figure 4). The reasons for the bias are unknown, but we hypothesize a combination of errors in the model and satellite imagery.

The GESE-CDOM showed a better correspondence with surface in situ CDOM measurements than with remote sensing retrievals (Figure 5). The correlation coefficient between these time series for surface CDOM at 350, 380, and 400 nm are 0.96, 0.96, and 0.97, respectively, and, the model-data RMSE is 0.01, 0.009, and 0.007 m^{-1}, smaller than the surface CDOM uncertainties of 0.04 m^{-1}. The GESE-CDOM also captured the doubling in surface CDOM around 21 March 2008.

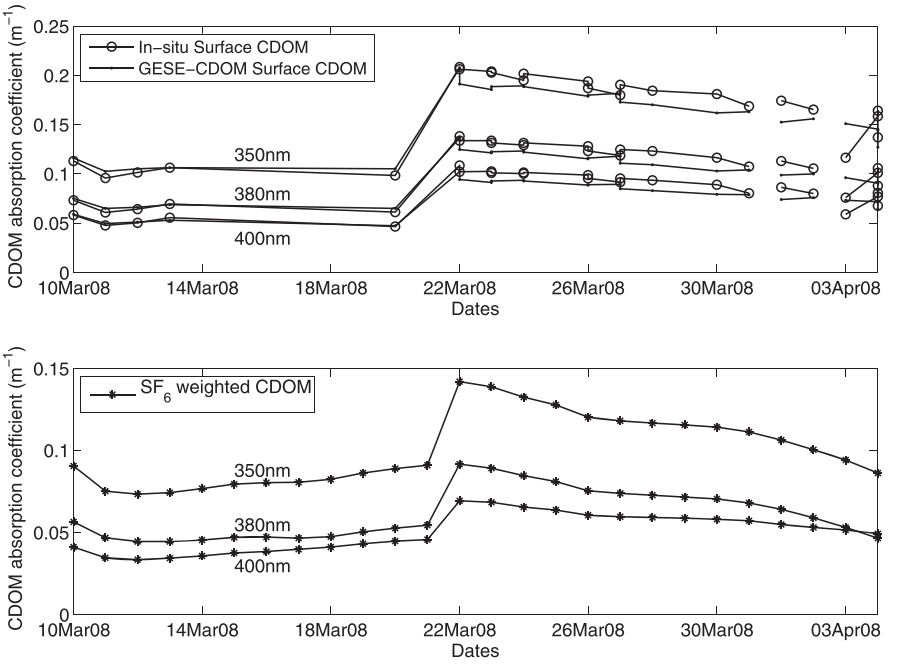

Figure 5. Comparison of the time series of SO GasEx in situ surface CDOM (circles) at 350, 380, and 400 nm with the corresponding GESE-CDOM surface CDOM values (dots). The samples are from the CTD stations shown in Figure 1.

The differences in the CDOM values along the cruise track between 20 March and 22 March 2008 are also seen in the CDOM profiles at 350 nm from in situ observations and GESE-CDOM (Figure 6). The CDOM values on 22 March 2008 are much higher compared to 20 March 2008 and the GESE-CDOM captures the change. The doubling in CDOM values between 20 and 22 March 2008 should not be seen as purely temporal change, however. It is the observation window that moved. The CDOM observations on 20 March 2008 are taken at a different location than the CDOM observations of 22 March 2008 as the cruise progressed. This doubling is because the SO GasEx cruise crosses a front between 20 March and 22 March 2008 (recall that the time series in Figure 5 is along the cruise track, not a Lagrangian trajectory). This front is visible in Figure 4 but that diagram presents averages from 21, 22, 24, and 27 March 2008. The shift from low surface CDOM values on 20 March 2008 (star symbol in Figure 4) to high values on 22 March 2008 (diamonds) is therefore unclear. The CDOM increase in Figure 5 is explained in the next section (see Figure 11).

The AVISO NADT, GHRSST, and CTD temperature and salinity data were plotted against the corresponding GESE-CDOM fields in Figure 6. These plots were very similar to the corresponding plots in *Dwivedi et al.* [2011] (their Figure 8). The in situ CDOM (at all wavelengths) and SF_6 values were also plotted against the corresponding GESE-CDOM fields in the present Figure 6. The correlation and RMSE between the in situ CDOM data and corresponding GESE-CDOM solution is 0.97 and 0.01 m^{-1}, respectively, whereas the correlation and RMSE between SF_6 data and the corresponding GESE-CDOM solution is 0.95 and 80 fmol L^{-1}, respectively. It is clear from the figures that most of the points on the scatter plots lie either on, or very close to, the best-fit line with only few points outside the uncertainty envelope. This is evidence of a good, although not perfect, fit of the state estimate to the data.

4.2. Effect of Entrainment, Photobleaching, Advection, and Diffusion on CDOM

We performed an experiment (called GESE-CDOM-EN0) to gauge the effect of thermocline entrainment in controlling the mixed-layer CDOM. In this experiment, we set the initial-condition CDOM values below the mixed-layer equal to the minimum ($\sim$0.02 m^{-1}) of all in situ CDOM observations for all wavelengths, everything else is the same as for GESE-CDOM. The vertical profile of initial CDOM for this experiment is shown in Figure 7. For GESE-CDOM-EN0, we carry out a forward run only (no adjustment of initial conditions).

During the SO GasEx it was observed that the CDOM values in the thermocline are lower than in the mixed-layer [Figure 2 in *Del Castillo and Miller*, 2011]. In experiment GESE-CDOM-EN0 we nearly eliminate the

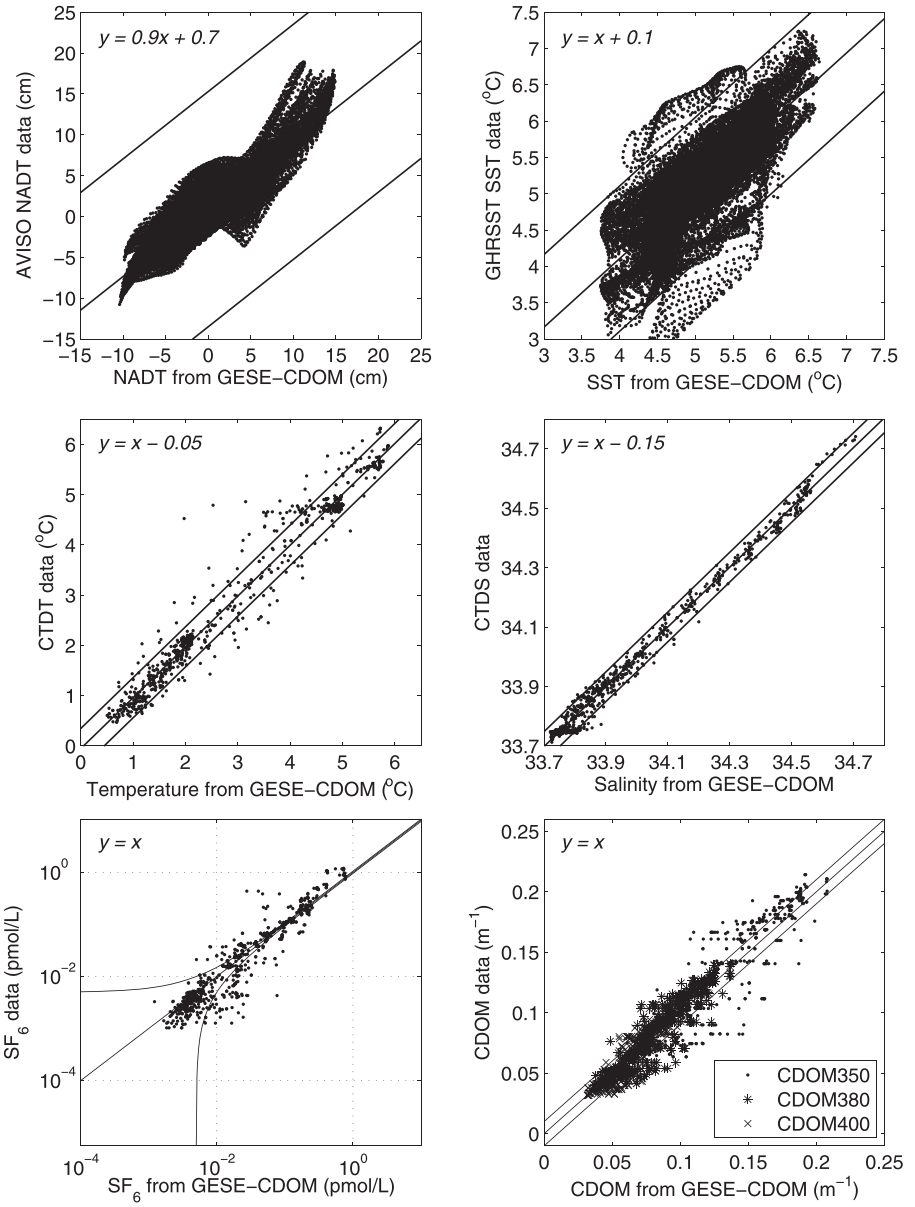

Figure 6. Scatter plots of: (top left) NADT (cm) data from AVISO against the GESE-CDOM solution; (top right) SST (°C) data from GHRSST against the GESE-CDOM solution; (middle left) CTD temperature (°C) data against the GESE-CDOM solution; (middle right) CTD salinity data against the GESE-CDOM solution; (bottom left) in situ SF_6 (pmol/L) data against the GESE-CDOM solution (note the logarithmic scale), and; (bottom right) in situ CDOM (m^{-1}) data against the GESE-CDOM solution. These results are for all 26 days of the state estimate. Lines above and below the best fit line in each plot mark the envelope defined by the average uncertainties. The best fit linear regression equation for each plot is written in the top left corner. The slopes of the best-fit lines are very close to 1, and the intercepts are also very small.

thermocline entrainment CDOM source (very low CDOM in the thermocline). Therefore, the mixed-layer CDOM values from this experiment are lower than in the GESE-CDOM experiment. The total cost function of the GESE-CDOM-EN0 experiment increases by a factor of 1.72, compared to GESE-CDOM. The ratio of CDOM and SCDOM costs compared to GESE-CDOM is summarized in Table 3 for each wavelength. The table shows that the normalized surface CDOM costs do not change much in the GESE-CDOM-EN0 experiment although they are slightly smaller. The normalized interior CDOM costs in the GESE-CDOM-EN0 experiment at each wavelength have higher values, however. This is not surprising because the GESE-CDOM-EN0 experiment starts with very different initial CDOM values below the mixed-layer. Thus, there will be greater misfit in the CDOM values below the mixed-layer in the GESE-CDOM-EN0 experiment than in the mixed-layer and at the

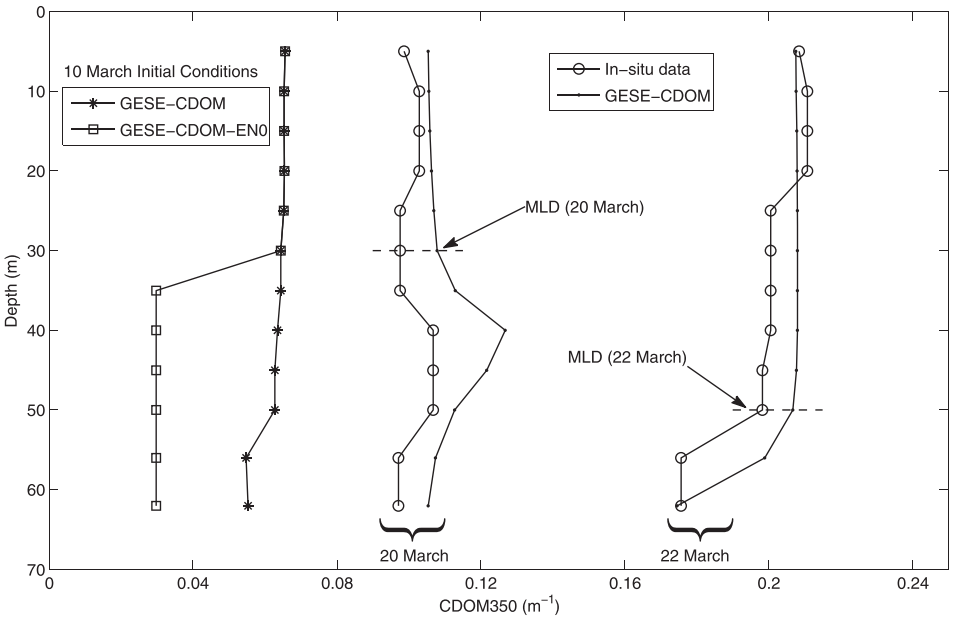

Figure 7. Comparison of the in situ CDOM profiles (circles) with the corresponding GESE-CDOM profiles (dots) at 350 nm on 20 March 2008 [37.78°W, 50.95°S] and 22 March 2008 [38.38°W, 51.15°S]. The CDOM350 initial condition at [38.05°W, 51.47°S] for the GESE-CDOM (stars), and GESE-CDOM-EN0 (squares) perturbation experiments are also shown.

surface. Indeed, the mixed-layer CDOM values in the GESE-CDOM-EN0 experiment remain closer to the GESE-CDOM values because both the experiments have the same initial mixed-layer CDOM values

The time averaged mixed-layer CDOM differences for 350 nm wavelength between GESE-CDOM-EN0 and GESE-CDOM are shown in Figure 8 (top left plot). The differences at 380 nm, and 400 nm are similar (not shown). The mixed-layer CDOM differences are negative because entrainment of lower CDOM thermocline waters reduces the mixed-layer CDOM. The northwest to southeast frontal region has the greatest differences indicating relatively strong entrainment there.

To assess the contribution of photodegradation in controlling the mixed-layer CDOM, we perform another perturbation experiment where the effect of photodegradation is ignored ($E = 0$ in (2); the experiment is called GESE-CDOM-E0. Everything else is the same as in the GESE-CDOM experiment. The total cost function in this case (GESE-CDOM-E0) increases by a factor of 1.14 compared to GESE-CDOM. The normalized CDOM and SCDOM costs at each wavelength for this experiment also increased (Table 3). The increases are not the same for each wavelength, however. They are larger for 380 nm than for 350 and 400 nm. This result suggests that the surface solar irradiance has a dominant role at 380 nm. This is an unexpected result because, based on the CDOM photodegradation action spectra, the greatest effect of photobleaching should be at the shortest wavelength (350 nm) [*Osburn et al.*, 2001; *Ayoub et al.*, 2009]. It may be due to wavelength dependent error in our CDOM photobleaching model (e.g., due to uncertainty in the value of σ_P or k at 380 nm, or because light at 350 nm is strongly attenuated). The spatial mixed-layer differences between GESE-CDOM and GESE-CDOM-E0 are shown in Figure 8 (top right plot). In the absence of photobleaching, the mixed-layer CDOM values increase, as expected. Photobleaching is most effective in the northeast of the domain where the SST is higher on average (Figure 2), although the spatial variations are less strong

Table 3. Cost Function Values for the Three Experiments With Perturbed CDOM Initial Conditions[a]

Experiment	Total	CDOM350	CDOM380	CDOM400	SCDOM350	SCDOM380	SCDOM400
GESE-CDOM-EN0	1.72	12.60	12.30	8.92	0.89	0.94	0.84
GESE-CDOM-E0	1.14	1.70	3.7	1.10	1.20	1.50	1.02
GESE-CDOM-AD0	5.34	30.20	36.34	28.10	1.30	1.35	1.18
GESE-CDOM-ADDI0	5.58	32.69	39.13	30.22	1.29	1.36	1.16

[a]The cost values are normalized by the corresponding GESE-CDOM costs.

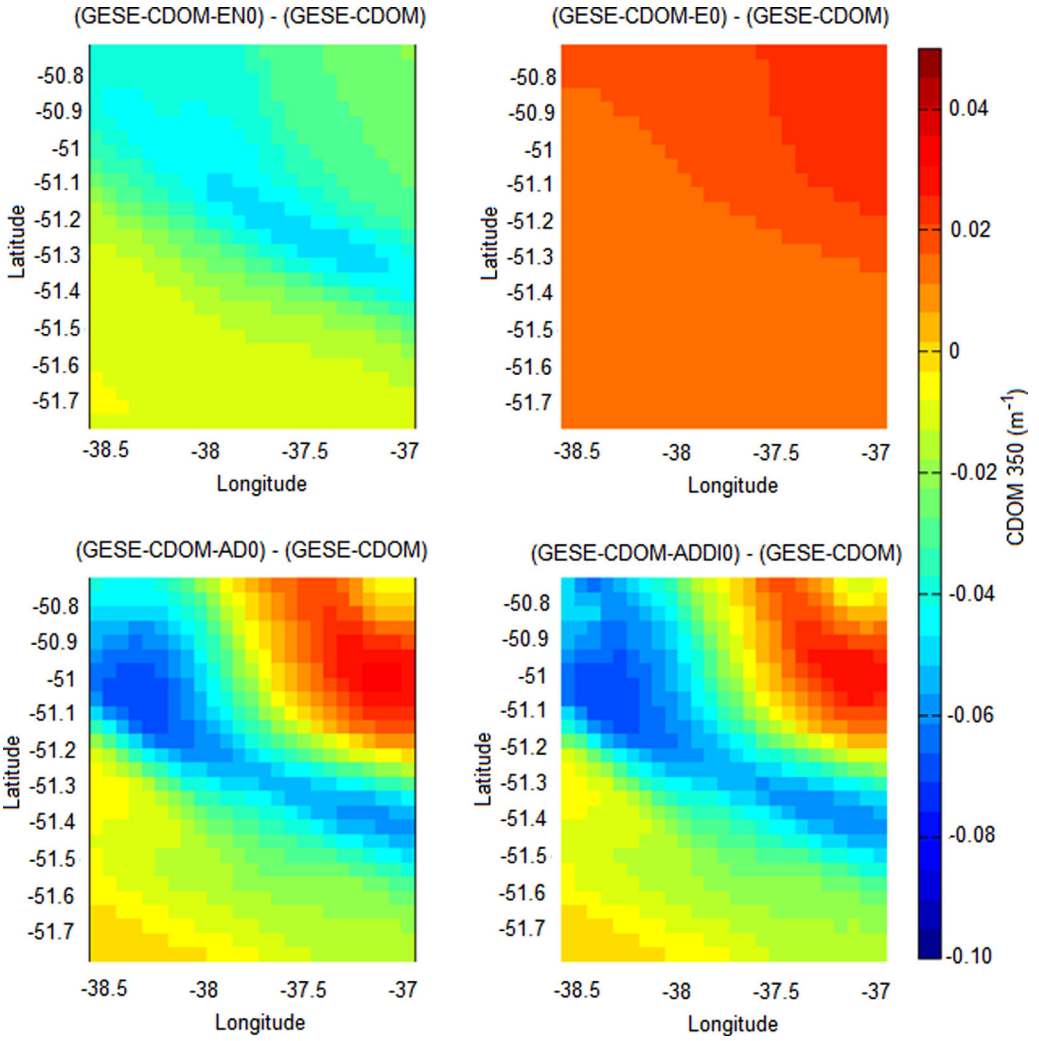

Figure 8. Time average spatial mixed-layer CDOM differences between GESE-CDOM and (i) GESE-CDOM-EN0 (top left plot), (ii) GESE-CDOM-E0 (top right plot), (iii) GESE-CDOM-AD0 (bottom left plot), and (iv) GESE-CDOM-ADDI0 (bottom right plot) for 350 nm wavelength.

than those caused by entrainment (compare to experiment GESE-CDOM-EN0). It causes changes of similar magnitude as entrainment in experiment GESE-CDOM-EN0. The CDOM differences are higher at 380 nm compared to 350 and 400 nm.

The contribution of horizontal advection to controlling the mixed-layer CDOM is assessed by performing another forward run (GESE-CDOM-AD0) with zero advection of CDOM; everything else is the same as in the GESE-CDOM experiment. The total cost function in this case increases by a factor of 5.34 compared to GESE-CDOM. The increase in normalized CDOM and SCDOM costs at each wavelength in the GESE-CDOM-AD0 experiment is also higher compared to the GESE-CDOM-EN0 and GESE-CDOM-E0 experiments (Table 3). The spatial mixed-layer differences between GESE-CDOM and GESE-CDOM-AD0 are shown in Figure 8 (bottom left plot). In the absence of advection, the mixed-layer CDOM values decrease except in the northeast of the domain where they increase. The frontal area has relatively higher mixed-layer CDOM differences compared to other locations, as in experiment GESE-CDOM-EN0.

To quantify the role of horizontal diffusive mixing in controlling the mixed-layer CDOM, we perform another forward run (GESE-CDOM-ADDI0) where both advection and horizontal diffusion of CDOM are set to zero; everything else is the same as in the GESE-CDOM experiment. The total cost function in this case increases by a factor of 5.58 compared to GESE-CDOM. The increase in normalized CDOM costs at each wavelength in the GESE-CDOM-ADDI0 experiment is highest compared to all other experiments (Table 3). The normalized

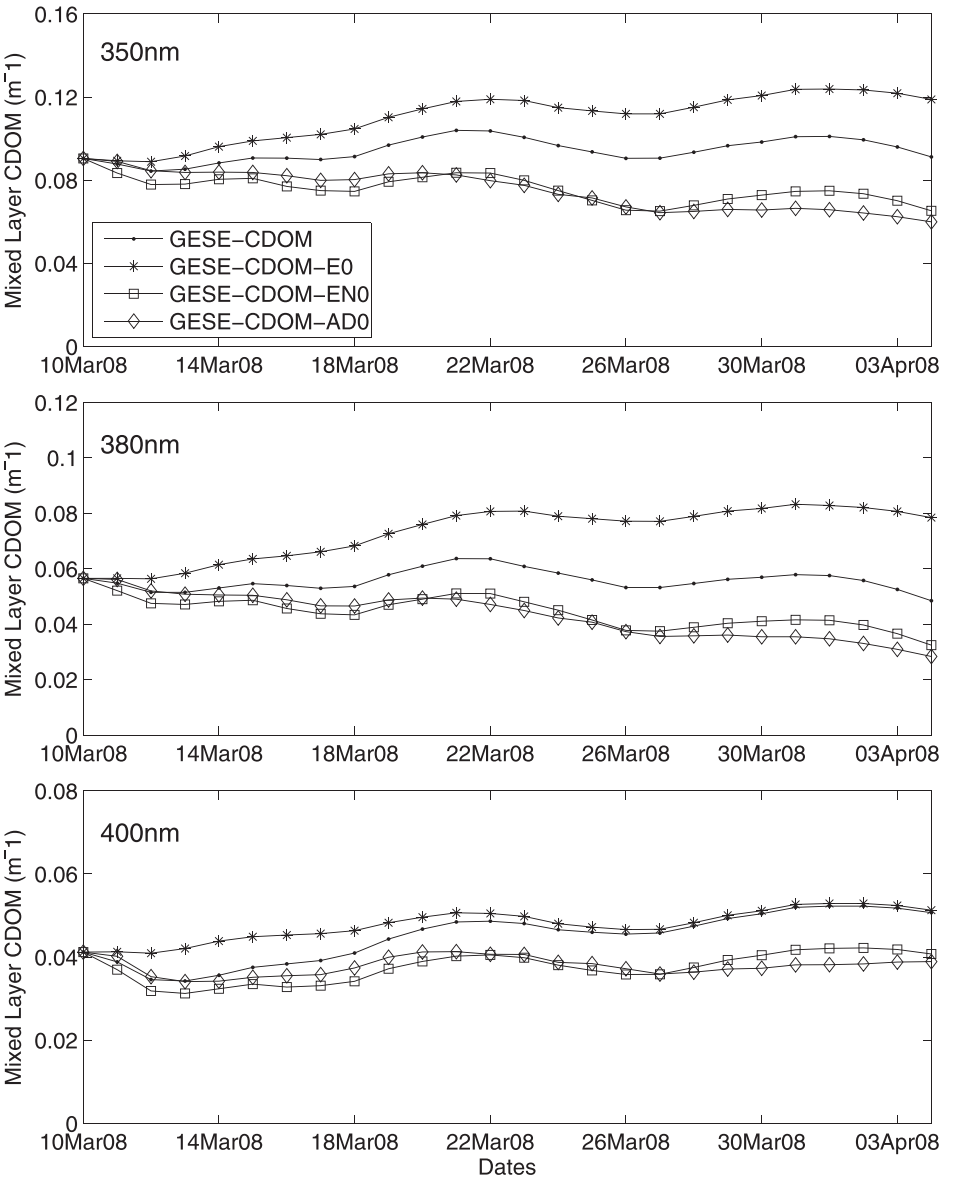

Figure 9. Time series of the mixed-layer CDOM values spatially averaged over the SO GasEx region obtained from the GESE-CDOM (dots), GESE-CDOM-E0 (stars), GESE-CDOM-EN0 (squares), GESE-CDOM-AD0 (diamonds), and GESE-CDOM-ADDI0 (circles) experiments.

SCDOM costs of the GESE-CDOM-ADDI0 experiment at each wavelength are nearly the same as in the GESE-CDOM-AD0 experiment. The spatial mixed-layer differences between GESE-CDOM and GESE-CDOM-ADDI0 are shown in Figure 8 (bottom right plot). In the absence of advection and diffusion (GESE-CDOM-ADDI0), the mixed-layer CDOM values change in the same way as in the absence of advection (GESE-CDOM-AD0): the differences between the two experiments are very small. Thus, horizontal diffusive mixing has very little role in controlling the mixed-layer CDOM compared to entrainment, photobleaching, and advection.

In Figure 9, we compared the time series of the mixed-layer CDOM values spatially averaged over the SO GasEx region (not along the cruise track) obtained from the GESE-CDOM, and the four perturbation experiments. The figure shows that for 350 and 380 nm wavelengths, the photobleaching experiment (GESE-CDOM-E0) increased the mixed-layer CDOM, whereas the entrainment (GESE-CDOM-EN0), advection (GESE-CDOM-AD0), and advection-diffusion (GESE-CDOM-ADDI0) experiments decreased it by a similar amount. The decrease in the mixed-layer CDOM is highest when advection and diffusion are switched off. The mixed-layer CDOM time variations in Figure 9 are similar among all the experiments.

The behavior at 400 nm in Figure 9 is surprising because for the first 5 days there is little impact of entrainment and advection (GESE-CDOM, GESE-CDOM-EN0, GESE-CDOM-AD0, and GESE-CDOM-ADDI0 are close to each other). Thereafter the impact of entrainment, advection, and advection-diffusion increases while that of photobleaching decreases. The photobleaching sink is locally sign-definite and hence the GESE-CDOM and GESE-CDOM-E0 curves in Figure 9 should apparently always diverge. This behavior is seen at 350 and 380 nm, but not at 400 nm. We do not have a good explanation about the lack of divergence at 400 nm shown in Figure 9, which suggests that photodegradation at 400 nm was limited after 22 March 2008. As suggested above, this effect could also be the result of confounding errors in our treatment of CDOM like the extrapolation to shorter wavelength based on averaged spectral slope, and uncertainty in the values of σ_P or k. These uncertainties will be addressed in future work.

We computed the *e*-folding rates for the differences between the base experiment and the perturbation experiments (shown in Figure 9) to quantify the averaged photodegradation, entrainment, advection, and advection-diffusion timescales. We found that the differences between the experiments were well fitted by an exponential curve for each wavelength. The exponents for the photodegradation, entrainment, advection, and advection-diffusion experiments were 0.065, 0.055, 0.084, and 0.089 d^{-1}, respectively. Thus, we found that the timescales corresponding to photodegradation, entrainment, advection, and advection-diffusion processes are 15, 18, 12, and 11 days, respectively, during the SO GasEx experiment.

To explore the reasons for CDOM doubling around 21 March 2008 (Figure 5), we related the CDOM variability with mixed-layer depth (MLD) variability. The MLD is defined as the depth where the first distinguishable decrease in the quasi-homogeneous profile of temperature is observed from its surface value. We use the *Lorbacher et al*. [2006] criterion to compute the MLD using the temperature field. This criterion is based on the shallowest extreme curvature of the near surface layer temperature profiles. We show in Figure 10 the space-time MLD from GESE-CDOM for all days of assimilation from 10 March to 4 April 2008. The GESE-CDOM MLD space-time variations are similar to those of *Dwivedi et al*. [2011] (their Figure 9). The space-time correlation between the GESE-CDOM and the GESE MLD is 0.8. The space-time averaged MLD from the GESE-CDOM experiment is 39 ± 8 m whereas the GESE value was 38 ± 8 m. In both estimates, the MLD deepens over the cruise period, although there were differences between the GESE-CDOM and GESE MLD fields. These differences indicated that the CDOM and SF_6 data in the GESE-CDOM solution are influencing the estimate of the temperature field, and hence the MLD estimate.

The corresponding space-time variability of CDOM350 averaged over the mixed-layer is shown in Figure 11. It is clear from the figure that the CDOM350 values are lowest in the southwest during the entire cruise period (as in Figure 4). During the first few days of the cruise high CDOM350 values are seen only in the northern part of the SO GasEx domain but later, they appear throughout the northern and central part of the domain. Isolated parcels of high CDOM can be seen to propagate coherently across the region, for example, from 10 to 23 March 2008. The correlation between the GESE-CDOM MLD at the SO GasEx stations and the corresponding mixed-layer CDOM350 values is 0.7. The MLD and mixed-layer CDOM350 values at the SO GasEx stations are shown in Figure 12. The figure shows that the CDOM at the SO GasEx stations increased as the mixed-layer deepens and vice versa. Further, the doubling of CDOM around 21 March 2008 (in Figures 5 and 11) was associated with the sharp increase in MLD around the same time (see e.g., a difference of nearly 20 m in MLD on 20 March and 22 March 2008 in Figure 6). The abrupt mixed-layer deepening around 21 March 2008 (during 21–26 March 2008) at the SST front is clearly seen from Figure 10. The mixed-layer deepening across the front in Figure 10 was also closely correlated with the entrainment and advection changes across the front in Figure 8: the deeper mixing reduced CDOM by entrainment of thermocline water, but this effect was overwhelmed by the increase in mixed-layer CDOM due to convergence of advective CDOM flux.

4.3. Kinematics of the SF_6 Tracer

The space-time variability of the deliberately released SF_6 tracer is shown in Figure 11. The center of the SF_6 patch nearly coincided with the SO GasEx stations indicating that the ship followed the patch closely. The total amount of SF_6 (obtained by integrating the SF_6 concentration over volume) during the SO GasEx period is shown in Figure 13 (top plot) as a function of time. The GESE-CDOM SF_6 mass was highest (1.24 mol) on 21 March 2008 and it decreased to 0.035 mol on 4 April 2008. During the SO GasEx approximately

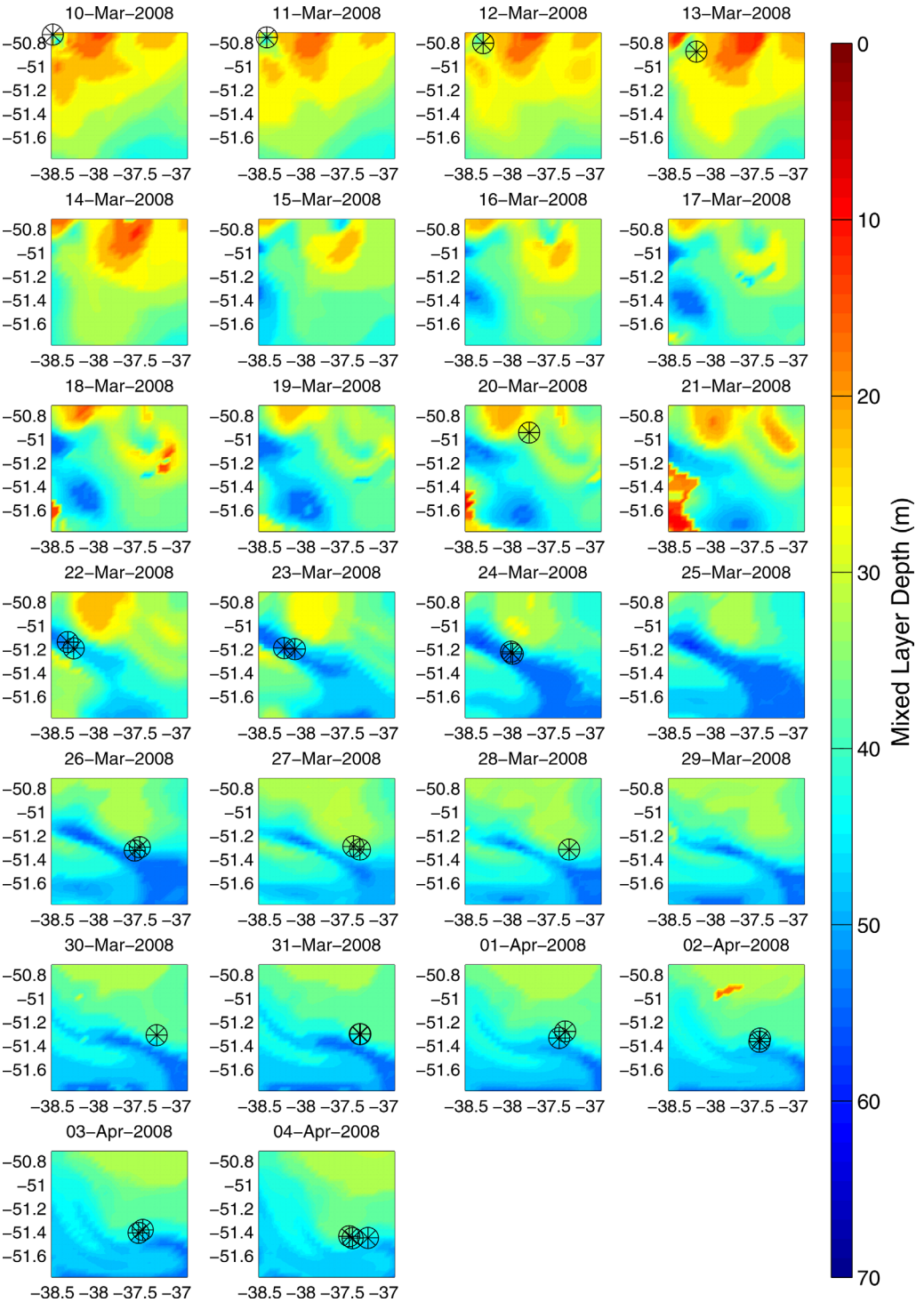

Figure 10. GESE-CDOM mixed-layer depth (m) for 12 GMT on 10 March to 4 April 2008. The symbols represent the SO GasEx cruise stations.

1.3 mol of SF_6 was injected in the ocean on 21 March 2008. Thus the GESE-CDOM SF_6 mass on 21 March 2008 compared well with the injected SF_6 mass. *Ho et al.* [2011] demonstrates that small-scale filamentary structures exist in the SF_6 data. The GESE-CDOM SF_6 field does not resolve these filaments as the numerical model has a horizontal grid spacing of approximately 4 km, which is too coarse to capture fine scale filament structure. Some of the discrepancies seen in Figure 13 (top plot) could be caused by the filaments.

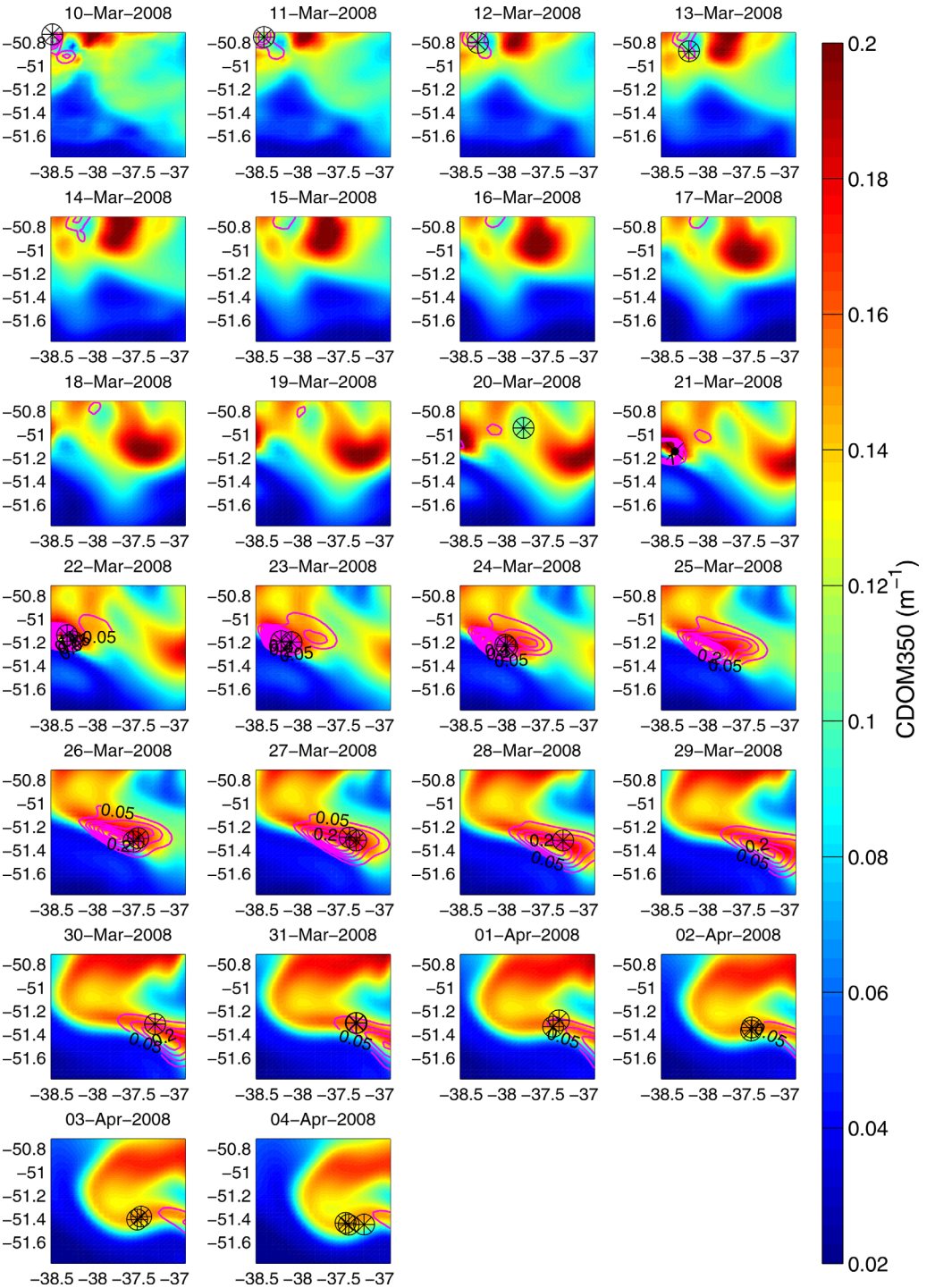

Figure 11. The GESE-CDOM mixed-layer CDOM350 (averaged over the MLD) on 10 March to 4 April 2008. The space-time variability of SF_6 is shown by contour plots (magenta). The symbols represent the SO GasEx cruise stations.

The kinematics of the deliberately released SF_6 tracer were controlled by the circulation and lateral diffusion. The stretching and dispersal of the tracer, after an initial period of adjustment, may be quantified by fitting the SF_6 contours to a Gaussian ellipse [*Abraham et al.*, 2000; *Xiu and Chai*, 2010]. Following a few days of patch expansion, the length (major axis) of the fitted ellipse increased exponentially with time at a rate γ, which measures the strain rate in the two-dimensional divergenceless flow. The ellipse width (minor axis) remained nearly constant at $(K/\gamma)^{1/2}$ because the thinning effect of strain balances the widening effect of

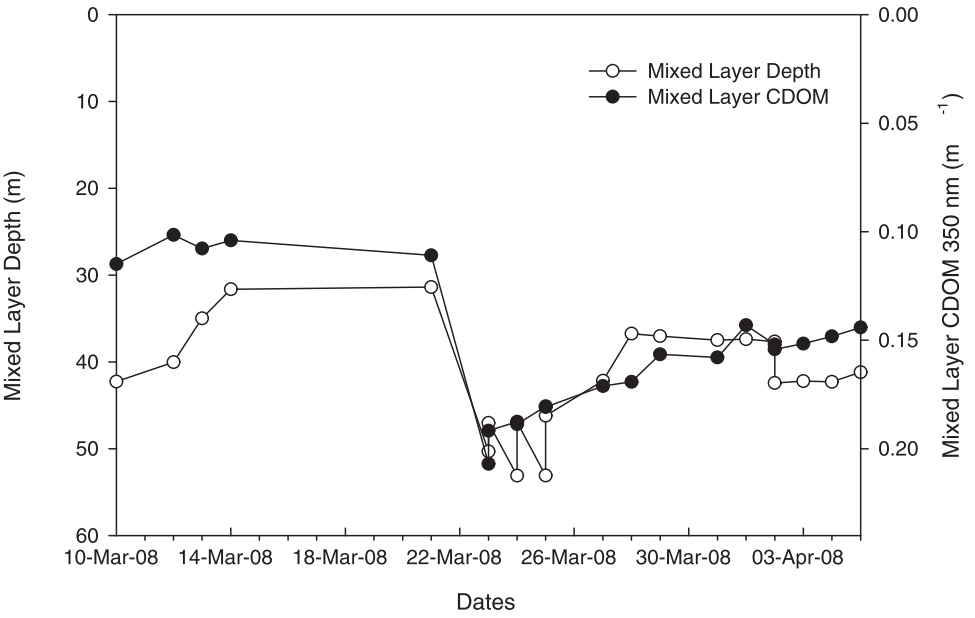

Figure 12. GESE-CDOM mixed-layer depth (m) and mixed-layer CDOM350 at the SO GasEx station locations.

diffusion K [*Abraham et al.*, 2000]. To estimate γ and K, we computed the length and width of the SF_6 tracer patch between 23 and 28 March 2008 by fitting Gaussian ellipses on each day. Fitting the Gaussian ellipses on the SF_6 tracer patch from the 2nd day to the 8th day after its deliberate release has been found to be sufficient to make a robust estimate of γ and K [*Abraham et al.*, 2000; *Law et al.*, 2003, 2006]. The effective strain rate γ was 0.14 d^{-1} (1.62×10^{-6} s^{-1}), whereas, the horizontal diffusivity K was 15 m^2 s^{-1}. This effective strain rate was similar ($8 \pm 3 \times 10^{-7}$ s^{-1}) to that determined by *Abraham et al.* [2000] for a different region [134°E–146°E; 57°S −62°S] in the Southern Ocean. The effective strain rate found here was higher than the 5.8×10^{-7} s^{-1} calculated using a generic model of mesoscale turbulence [*Haidvogel and Keffer*, 1984]. However, and as determined by a tracer release ($3 \pm 0.5 \times 10^{-7}$ s^{-1}) in the subtropical ocean interior [*Ledwell et al.*, 1998]. Similarly, the GESE-CDOM horizontal diffusivity was higher compared to estimates of 4 ± 2 m^2 s^{-1} by *Abraham et al.* [2000]. It falls in the same range as obtained in dye-release experiments (2–16 m^2 s^{-1}) performed in shelf seas [*Okubo*, 1971], and within an eddy in the North Atlantic Ocean (22 ± 10 m^2 s^{-1}) during an open ocean surface SF_6 release [*Martin et al.*, 2001]. The difference among these experiments might be due to different observational time lengths, different initial release area, and different physical conditions related to the high spatial and temporal variability of strain in ocean currents [*Law et al.*, 2006; *Xiu and Chai*, 2010].

In Figure 13 (bottom plot), we show the SF_6-weighted CDOM fields at each wavelength during the assimilation period. The SF_6-weighted CDOM fields are obtained by dividing the surface integral of the product of the CDOM field and the deliberately released SF_6 field (on each day and at each wavelength) by the integral of the deliberately released SF_6 field for that day. Using the SF_6 as a weighting function to integrate the CDOM fields gives a Lagrangian view on the CDOM variability: it focuses attention on the CDOM following the SF_6 patch as it moves and spreads. Clearly, these time series resemble the surface CDOM fields (shown in Figure 5) and capture most of its time variations because the ship followed the patch reasonably well. We, therefore, surmise that the Lagrangian horizontal advection of waters associated with the SST front around 21 March 2008 was mainly responsible for the doubling of surface CDOM during that time.

5. Conclusions

Our high-resolution, regional data assimilation system successfully fit in situ and satellite data and provided a three-dimensional time-varying estimate of physical fields, CDOM and SF_6 tracers in the locale of SO GasEx. To the best of our knowledge this is the first Southern Ocean state estimation involving CDOM and

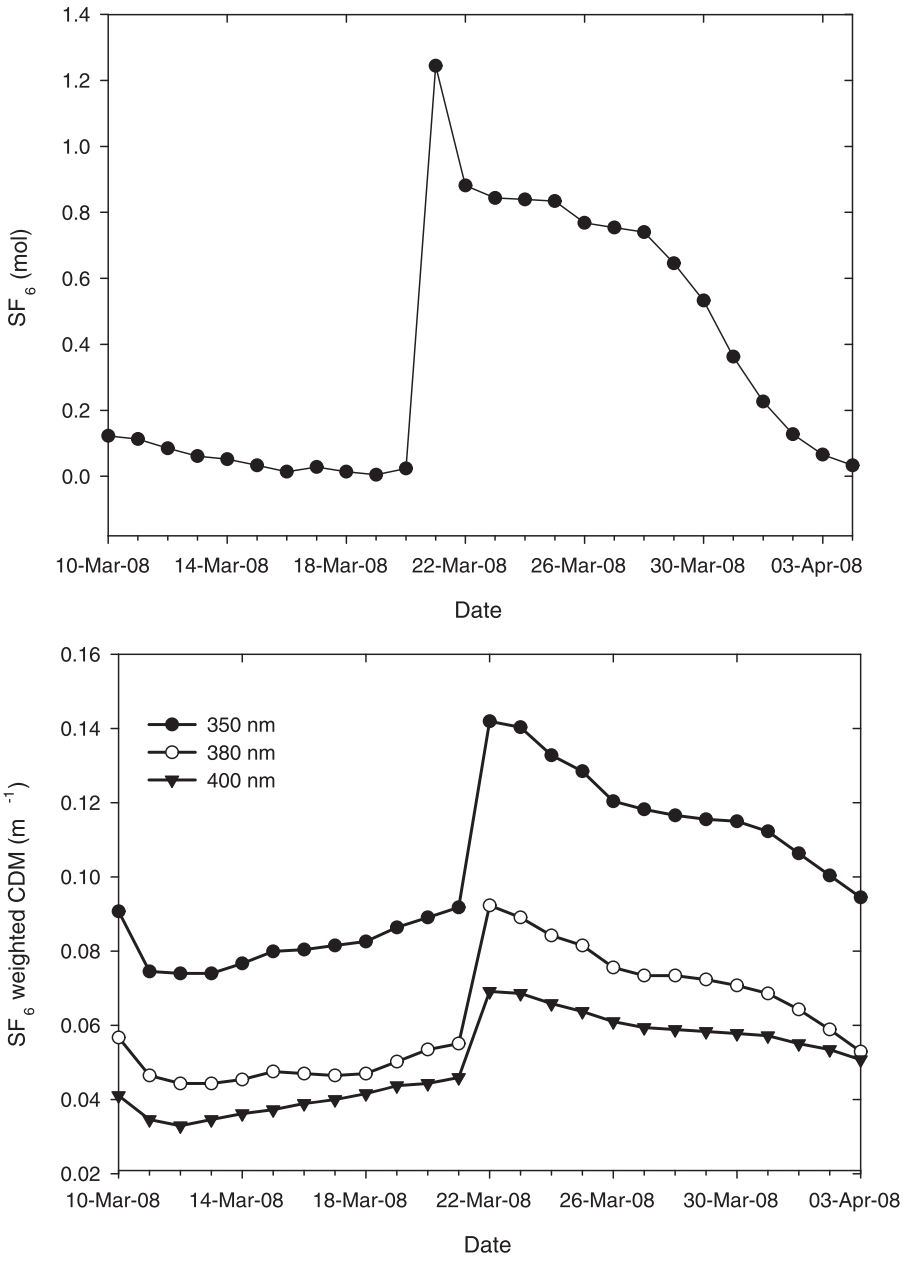

Figure 13. (top plot) total amount of SF_6 (mole) as a function of time; (bottom plot) SF_6 weighted CDOM absorption coefficient (m^{-1}) as a function of time for each wavelength (see text).

SF_6. The photodegradation of CDOM and surface transport of SF_6 were explicitly modeled for this purpose. Our assimilation setup captured the doubling in mixed-layer CDOM along the cruise track around 21 March 2008, even though it did not include any biological source or sink term. The doubling of CDOM was explained by the ship crossing a front between 20 and 22 March 2008 and the associated mixed-layer deepening. The effect of entrainment, advection, and photobleaching were quantified to better understand the spatiotemporal variability of the SO GasEx mixed-layer CDOM. Different perturbation experiments were performed for this purpose. It was shown that entrainment of lower CDOM thermocline waters reduced the mixed-layer CDOM with a characteristic time scale of 18 days. The effect of entrainment is greater in the frontal region compared to other locations in the SO GasEx domain. The photobleaching is a sink of mixed-layer CDOM and decreases its abundance with a characteristic time scale of 16 days. Convergence of advective fluxes was a source of mixed-layer CDOM with a characteristic time scale of 12 days. This advective

CDOM source was higher in the frontal region compared to other locations and exceeded the effects of entrainment and photobleaching, which have similar sizes. The thermocline entrainment, lateral advection, and photobleaching collectively explained most of the mixed-layer CDOM variability during the SO GasEx experiment and convergence of lateral diffusive fluxes was negligible. Biological sources and sinks of CDOM were also negligible over the six week SO Gas Ex cruise. An effective strain rate of 0.14 d^{-1}, and a horizontal diffusivity of 15 m^2 s^{-1} were inferred from the dispersal of SF_6 in the state estimate.

Future work should explore CDOM state estimation over longer periods and greater areas to understand processes controlling its abundance and distribution. It will also be interesting to include other biological compounds in future state estimates to infer information about their controlling processes. We found that this modeling technique can be very useful in future process studies as it provides reasonable estimates on the temporal and spatial evolution of circulation features (e.g., fronts, eddies) and aid in studies that involve tracer releases. Improved ship-to-shore communications and the deployment of supercomputers onboard research vessels should allow for the implementation of this method during research cruises.

Acknowledgments

This work was supported by NASA (06-0BB06-0019) and NOAA (NA07OAR4310113). We are grateful to the JHU-APL for providing computational resources. The in situ data were kindly provided by the SO GasEx community. The NCEP reanalysis data are provided by the NOAA/OAR/ESRL PSD, Boulder, Colorado, USA, from their website at http://www.esrl.noaa.gov/psd/. The blended sea winds data are provided by the National Climate Data Center (NCDC) Satellite Data Services, from their website at http://www.ncdc.noaa.gov/oa/rsad/seawinds.html/. The NADT altimeter products were produced by Ssalto/Duacs and distributed by Aviso, with support from Cnes (http://www.aviso.oceanobs.com/duacs/). We thank the global ocean data assimilation experiment (GODAE) high-resolution sea surface temperature pilot project for providing L4 gridded SST data.

References

Abraham, E. R., C. S. Law, P. W. Boyd, S. J. Lavender, M. T. Maldonado, and A. R. Bowie (2000), Importance of stirring in the development of an iron-fertilized phytoplankton bloom, *Nature*, *407*, 727–730.

Adcroft, A., et al. (2009), MITgcm user's manual (online documentation), MIT/EAPS. [Available at http://mitgcm.org/r2_manual/latest/online_documents/manual.html.]

Atkinson, A., M. J. Whitehouse, J. Priddle, G. C. Cripps, P. Ward, and M. A. Brandon (2001), South Georgia, Antarctica: A productive, cold water, pelagic ecosystem, *Mar. Ecol. Prog. Ser.*, *216*, 279–308.

Ayoub, L., P. Hallock, and P. Coble (2009), Colored dissolved organic material increases resiliency of coral reefs by controlling exposure to UVR, in *Proceedings of the 11*th *International Coral Reef Symposium, Ft. Lauderdale, Florida*, pp. 572–576.

Blough, N. V., and R. Del Vecchio (2002), Chromophoric DOM in the Coastal Environment, in *Biogeochemistry of Marine Dissolved Organic Matter*, edited by D. A. Hansell and C. A. Carlson, Academic, San Diego.

Coble, P.G. (2007), Marine optical biogeochemistry: The chemistry of ocean color, *Chem. Rev., 107*, 402–418, doi:10.1021/cr050350.

Del Castillo, C. E., and R. L. Miller (2011), Horizontal and vertical distributions of colored dissolved organic matter during the Southern Ocean Gas Exchange Experiment, *J. Geophys. Res.*, *116*, C00F07, doi:10.1029/2010JC006781.

Del Castillo, C. E., P. G. Coble, J. M. Morell, J. M. Lopez, and J. E. Corredor (1999), Analysis of the optical properties of the Orinoco River plume by absorption and fluorescence spectroscopy, *Mar. Chem.*, *66*, 35–51.

Del Vecchio, R., and N. V. Blough (2002), Photobleaching of chromophoric dissolved organic matter in natural waters: Kinetics and modeling, *Mar. Chem.*, *78*, 231–253.

Dwivedi, S., T. W. N. Haine, and C. E. Del Castillo (2011), Upper ocean state estimation in the Southern Ocean Gas Exchange Experiment region using the four-dimensional variational technique, *J. Geophys. Res.*, *116*, C00F02, doi:10.1029/2009JC005615.

Gregg, W. W., and N. W. Casey (2009), Skill assessment of a spectral ocean-atmosphere radiative model, *J. Mar. Syst.*, *76*, 49–63.

Haidvogel, D. B., and T. Keffer (1984), Tracer dispersal by mid-ocean mesoscale eddies. Part I: Ensemble statistics, *Dyn. Atmos. Oceans*, *8*, 1–40.

Ho, D. T., C. S. Law, M. J. Smith, P. Schlosser, M. Harvey, and P. Hill (2006), Measurements of air-sea gas exchange at high wind speeds in the Southern Ocean: Implications for global parameterizations, *Geophys. Res. Lett.*, *33*, L16611, doi:10.1029/2006GL026817.

Ho, D. T., C. L. Sabine, D. Hebert, D. S. Ullman, R. Wanninkhof, R. C. Hamme, P. G. Strutton, B. Hales, J. B. Edson, and B. R. Hargreaves (2011), Southern Ocean Gas Exchange Experiment: Setting the stage, *J. Geophys. Res.*, *116*, C00F08, doi:10.1029/2010JC006852.

Jørgensen, L., C. A. Stedmon, T. Kragh, S. Markager, M. Middelboe, and M. Søndergaard (2011), Global trends in the fluorescence characteristics and distribution of marine dissolved organic matter, *Mar. Chem.*, *126*, 139–148.

Kalnay, E., et al. (1996), The NCEP/NCAR re-analysis project, *Bull. Am. Meteorol. Soc.*, *77*, 437–471.

Korb, R. E., and M. Whitehouse (2004), Contrasting primary production regimes around South Georgia, Southern Ocean: Large blooms versus high nutrient, low chlorophyll waters, *Deep Sea Res., Part I*, *51*, 721–738.

Law, C. S., E. R. Abraham, A. J. Watson, and M. I. Liddicoat (2003), Vertical eddy diffusion and nutrient supply to the surface mixed layer of the Antarctic Circumpolar Current, *J. Geophys. Res.*, *108*(C8), 3272, doi:10.1029/2002JC001604.

Law, C. S., et al. (2006), Patch evolution and the biogeochemical impact of entrainment during an iron fertilisation experiment in the sub-Arctic Pacific, *Deep Sea Res., Part II*, *53*, 2012–2033.

Ledwell, J. R., A. J. Watson, and C. S. Law (1998), Mixing of a tracer in the pycnocline, *J. Geophys. Res.*, *103*, 21,499–21,529.

Lee, Z. P., K. L. Carder, and R. A. Arnone (2002), Deriving inherent optical properties from water color: A multi-band quasi-analytical algorithm for optically deep waters, *Appl. Opt.*, *41*, 5755–5772.

Lorbacher, K., D. Dommenget, P. P. Niiler, and A. Köhl (2006), Ocean mixed layer depth: A subsurface proxy of ocean-atmosphere variability, *J. Geophys. Res.*, *111*, C07010, doi:10.1029/2003JC002157.

Martin, A. P., K. J. Richards, C. S. Law, and M. I. Liddicoat (2001), Horizontal dispersion within an anticyclonic mesoscale eddy, *Deep Sea Res., Part II*, *48*, 739–755.

Meskhidze, N., A. Nenes, W. L. Chameides, C. Luo, and N. Mahowald (2007), Atlantic Southern Ocean productivity: Fertilization from above or below?, *Global Biogeochem. Cycles*, *21*, GB2006, doi:10.1029/2006GB002711.

Miller, R. L., M. Belz, C. Del Castillo, and R. Trzaska (2002), Determining CDOM absorption spectra in diverse coastal environments using a multiple pathlength, liquid core waveguide system, *Cont. Shelf Res.*, *22*, 1301–1310.

Nelson, N. B., and D. A. Siegel, and A. F. Michaels (1998), Seasonal dynamics of colored dissolved material in the Sargasso Sea, *Deep Sea Res. I*, *45*, 931–957.

Nelson, N. B., D. A. Siegel, C. A. Carlson C. Swan, W. M. Smethie, and S. Khatiwala (2007), Hydrography of chromophoric dissolved organic matter in the North Antlantic, *Deep Sea Res. I*, *54*, 710–731.

Okubo, A. (1971), Oceanic diffusion diagrams, *Deep Sea Res. Oceanogr. Abstr.*, *18*, 789–802.

Osburn, C. L., H. E. Zagarese, D. P. Morris, B. R. Hargreaves, and W. E. Cravero (2001), Calculation of the spectral weighting functions for the solar photobleaching of chromophoric dissolved organic matter in temperate lakes, *Limnol. Oceanogr.*, *46*, 1455–1467.
Preisendorfer, R. W. (1976), *Hydrologic Optics*, vol. 5, pp. 255–259, U.S. Dep. of Commer., NOAA Environ. Res. Lab., Washington, D. C.
Reynolds, R. W., T. M. Smith, C. Liu, D. B. Chelton, K. S. Casey, and M. G. Schlax (2007), Daily high-resolution blended analyses for sea surface temperature, *J. Clim.*, *20*, 5473–5496.
Smith, R. C., and K. S. Baker (1981), Optical properties of the clearest natural waters (200–800 nm), *Appl. Opt.*, *20*, 177–184.
Smith, W., and D. Sandwell (1997), Global sea floor topography from satellite altimetry and sparse shipboard bathymetry, *Science*, *277*, 1956–1961.
Xiu, P., and F. Chai (2010), Modeling the effects of size on patch dynamics of an inert tracer, *Ocean Sci.*, *6*, 413–421.
Zhang, H.-M., J. J. Bates, and R. W. Reynolds (2006), Assessment of composite global sampling: Sea surface wind speed, *Geophys. Res. Lett.*, *33*, L17714, doi:10.1029/2006GL027086.
Zhu, W., Q. Yu, Y. Q. Tian, R. F. Chen, and G. B. Gardner (2011), Estimation of chromophoric dissolved organic matter in the Mississippi and Atchafalaya river plume regions using above surface hyperspectral remote sensing, *J. Geophys. Res.*, *116*, C02011, doi:10.1029/2010JC006523.

Erratum

In the originally published version of this article, the author's name was misspelled in the footer. This has since been corrected, and this version may be considered the authoritative version of record.